Nanoscale

PAPER

View Article Online
View Journal



Cite this: DOI: 10.1039/d5nr04486c

# How low-temperature welding affects the nanostructure of nanowire junctions

Matteo Ferliga, Davide Grazioli, Angelo Simone * and Lucia Nicola

Depending on the synthesis methods employed, nanowires for flexible electronics are either single crystals or possess a penta-twinned nanostructure. This nanostructure, along with the relative crystallographic orientation of the nanowires and the welding temperature, determines the degree of interpenetration between wires and the nanostructure of the junction. This study tracks, by means of atomistic simulations performed at various temperatures, the formation and evolution of the joint between pairs of nanowires. The results show that penta-twinned nanowires generally yield the greatest interpenetration between wires and the most significant nanostructural changes, driven by atomic diffusion facilitated by the presence of twin boundaries. In contrast, single-crystal nanowires can form, in specific orientations, nearly defect-free yet poorly interpenetrated junctions. While surface curvature is an important parameter that drives atomic diffusion and thus promotes interpenetration, it is the presence of twin boundaries that has a dominant role in triggering nanostructural variation in the nanowires during welding.

Received 25th October 2025,
Accepted 4th March 2026

DOI: 10.1039/d5nr04486c

rsc.li/nanoscale



## 1 Introduction

The rapid advancement of transparent and flexible electronic technologies has stimulated significant interest in nanomaterials, which are suitable for use as both active components and conductive interconnects in a wide range of devices, including energy harvesters,[12,43] batteries,[29] supercapacitors,[5] touch panels,[34] light-emitting diodes (LEDs),[42] and solar cells.[32] In this context, metallic nanowires[15,17,44,50] and carbon nanotubes (CNTs)[23,62] have been widely explored as alternatives to indium tin oxide (ITO). Although ITO remains the most widely adopted transparent conductor in commercial devices, it suffers from intrinsic brittleness that limits its suitability for flexible applications, as well as from concerns regarding indium supply and cost. By contrast, transparent electrodes based on metallic nanowire networks—particularly silver nanowires (AgNWs)—offer a favorable combination of electrical performance, mechanical flexibility, and compatibility with scalable, low-cost, solution-based fabrication processes.[15,16,35] The performance of such devices is critically determined by network properties such as electrical conductivity,[10,17] electrical homogeneity,[17,51] and electromechanical resilience.[18,25] Although these properties depend on both the intrinsic characteristics of the nanowires and the spatial organization of the network, inter-nanowire junctions often play a decisive role in determining the most performant configuration.[19] Consequently, junctions are key determinants of both the electrical and mechanical performance of the network, yet the mechanisms governing their formation and evolution remain poorly understood. Here, we use atomistic simulations to systematically explore how the nanostructure of silver nanowire junctions evolves. While previous studies have investigated nanowire pairs with fixed crystallography and specific orientations,[7,26,38,39,57] such cases do not capture the full range of junction configurations that can form in a network. The range of junction configurations that can arise in a network is determined by three key factors: the nanowire structure, which may be single-crystal (SC) or penta-twinned (PT); the deposition technique employed to assemble the nanowires onto the substrate, which determines their mutual orientation;[45] and the welding process conditions, in particular the temperature, which affects atomic diffusion and thus interpenetration.[10] PT nanowires generally show enhanced mechanical properties compared to SC nanowires,[40,48] but there is no clear evidence that they outperform SC nanowires in nanowire networks.[6,7,15,27,37,44,50,63]

Deposition techniques such as spin coating,[59] spray coating,[33] bar coating,[2] ink-jet printing,[61] and gravure printing[25] introduce a wide distribution of relative orientations between nanowires, which can affect the nanostructural evolution during welding. Radmilović *et al.*[49] experimentally showed that, for PT nanowires with a pentagonal cross-section, the junction is deeper when a facet of one nanowire contacts a twin plane of the other, rather than when two facets are in contact. Nian *et al.*[39] demonstrated through atomistic

*Department of Industrial Engineering, University of Padua, Via Venezia 1, 35131 Padua, Italy. E-mail: matteo.ferliga@unipd.it, davide.grazioli@unipd.it, angelo.simone@unipd.it, lucia.nicola@unipd.it*

simulations that junctions formed by perpendicularly crossed single-crystal nanowires can develop an ordered crystalline structure with a distinct grain boundary after welding. Nguyen *et al.*[38] also performed atomistic simulations and found that SC nanowires with a (001) orientation form stronger welded junctions, with shorter dislocation lengths, compared to those with (110) and (111) orientations. While these studies have explored specific nanowire orientations and their effects, a systematic analysis of how junction formation depends on the relative crystallographic orientation is still lacking.

Finally, welding conditions play a decisive role in shaping the final junction structure. Localized heating welding (LHW) processes, such as electron beam welding,[55] Joule heating,[30,54] and light-induced methods,[6,15,27,44] can be used to weld nanowires and form a network. These techniques ensure that only the junctions are affected by an increased temperature that induces welding, while the surrounding nanowire network remains at low temperature and thus unaltered. Although temperature is a key factor in welding, the literature does not report the temperatures reached at junctions during LHW. Garnett *et al.*[15] estimated that local temperatures must exceed 150 °C for their optical nanowelding process, while Peng *et al.*[46] analytically predicted junction temperatures of 435–445 °C during laser irradiation of Ag-nanoparticle films. In addition, Park *et al.*[44] numerically found that junction temperatures during plasmonic welding exceed the substrate temperature by approximately 300 °C. Although these estimates span a broad range, all reported values remain below the melting temperature, suggesting that junctions form *via* diffusion-assisted sintering without applied pressure. In the following, we will continue to use the term "welding" to refer to the process leading to the formation of the junction, although the temperatures involved are always maintained below the melting temperature.

In this work, we use atomistic simulations to systematically explore the evolution of silver nanowire junctions as a function of their initial nanostructure (single-crystal or penta-twinned), relative crystallographic orientation, and welding temperature. By considering a wide range of conditions, our results offer broader insight than previous studies and provide design-relevant guidelines for optimizing nanowire network performance.

# 2 Methods

## 2.1 Numerical simulations overview

We perform MD simulations to mimic low-temperature localized welding between individual pairs of NWs. The numerical simulations are performed using Ag NW pairs with either SC or PT nanostructure, characterized by non-coplanar, perpendicular longitudinal axes, as shown in Fig. 1. The relative orientation of the nanowires is defined through the angles $\theta_1$ and $\theta_2$ that express the relative rotations of $NW_1$ and $NW_2$ about their own longitudinal axes. The nanowires have diameter $d_w$ = 5 nm for circular cross-sections and $d_w$ = 5.4 nm for pentagonal ones. The effect of nanowire length was assessed

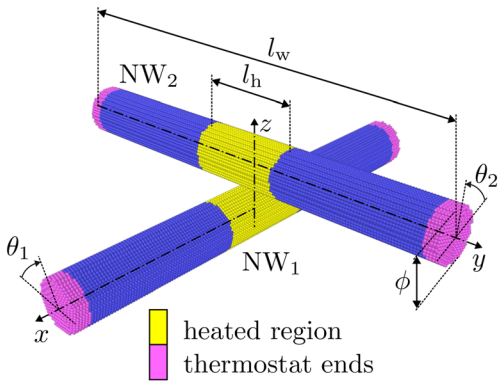


**Fig. 1** NW pair in a perpendicular arrangement. The yellow region denotes the atoms subject to heating, whereas the purple regions indicate the atoms kept at room temperature. Simulations are conducted for various values of the angles $\theta_1$ and $\theta_2$, as well as different target temperatures.

by considering $l_w$ in the range 25–90 nm, corresponding to aspect ratios $l_w/d_w \approx$ 5–18. Unless otherwise stated, the simulations reported in this work were performed for $d_w$ = 5 nm and $l_w$ = 45 nm. This choice is supported by additional simulations with $l_w \in \{20, 45, 90\}$ nm, which revealed negligible differences between the two longest wires. Periodic boundary conditions are applied at the ends of the NWs, corresponding to the simulation of a periodic array of junctions with axial spacing equal to the nanowire length, $l_w$. Localized heating-induced welding is simulated by raising the temperature of the group of atoms shown in yellow in Fig. 1 to the target temperature, $T_{target}$, while maintaining both ends of the NWs (represented by purple atoms) at room temperature. The bottom NW ($NW_1$) is assumed to adhere to a substrate, restricting its movement. This constraint is applied to all atoms within 5 Å of the bottom surface. The top NW ($NW_2$), positioned 1 nm away from the first, is free to deform.

All numerical simulations involve three stages: heating, holding, and cooling. During the heating stage, the temperature is increased from room temperature to the target temperature $T_{target}$, given as a fraction of the melting temperature of silver, $T_m$ = 962 °C. Temperature is kept at $T_{target}$ during the holding stage and brought back to ambient temperature in the cooling stage. The heating stage lasts 0.9 ns, whereas the post-welding stage includes a free cooling toward room temperature followed by relaxation, such that the overall post-welding duration (cooling plus relaxation) is 1.0 ns. The holding stage is the longest, lasting 75.9 ns, as an extended duration is required to ensure completion of the sintering process and attainment of the final configuration. The total duration of the welding process (heating–holding–post-welding) is thus 76.9 ns, significantly exceeding the timescales investigated in previous MD studies on NW welding (*e.g.*, 0.12 ns,[7] 0.4 ns,[26] 0.75 ns (ref. 39)). This extended simulation time is essential to capture all the nanostructural changes that occur within the junctions while being held at the target temperature. Regarding the range of target temperatures explored ($0.3T_m$,

$0.6T_m$ and $0.85T_m$), these values correspond to distinct diffusion regimes in terms of homologous temperature. At $0.3T_m$, diffusion is expected to be limited; at $0.6T_m$, diffusion becomes substantial while preserving the overall nanowire structure; and at $0.85T_m$, diffusion becomes very rapid, approaching conditions where morphological instabilities (*e.g.*, Rayleigh-type effects) may occur. These temperature ranges are consistent with *a posteriori* estimates reported in the experimental literature for localized welding processes.[15,44] In experiments, the junction temperature is typically reached locally and controlled indirectly through welding parameters (*e.g.*, illumination power/duration or current density and thermal coupling to the substrate), whereas in our MD simulations we prescribe $T_{target}/T_m$ to systematically probe different local thermal conditions and diffusion regimes.

To quantify the degree of interpenetration between the NWs, we define the interpenetration factor IF = $(h_0^z - h_f^z)/h_0^z$, where $h_0^z$ is the vertical component of the distance between the centers of mass of the NWs at the onset of the heating phase, and $h_f^z$ is the vertical component at any time step. The limiting cases of null and full penetration correspond to IF = 0 and IF = 1, respectively. Although neck size has been used in the literature[9,26] as a measure of nanowire connection, we prefer to opt for the IF, as determining the neck size for non-planar surfaces leads to ambiguity. For additional details on the IF the reader is referred to section 1 of the SI.

Atomic mobility in FCC crystals is strongly dependent on crystallographic orientation. Diffusion on {111} planes is generally more favorable, facilitated by mechanisms such as simple atomic exchange or chain-like processes.[1] In contrast, diffusion on {100} planes requires more complex mechanisms leading to significantly lower mobility.[28] This entails that diffusion, and thus interpenetration, can be more or less pronounced depending on the relative orientation of the nanowires, as shown in Fig. 1. In particular, there exist specific orientations, hereafter denoted as "notable", in which identical crystallographic planes face each other at the junction. These cases provide the lower and upper bounds of diffusivity and interpenetration in FCC crystals. However, they are rarely encountered in actual networks, where random orientations are most likely to occur. We will thus distinguish in the following between "notable" and "generic" orientations, the first defining limiting cases, *i.e.*, determining the lower and upper bounds, and the latter representing the majority of junctions in real nanowire networks.

In addition to crystallography and temperature, the local surface curvature at the junction can further modulate diffusion rates, and its role is specifically investigated in section 4.3.

### 2.2 Simulation details

To simulate a local heating process, we enforce a gradual temperature increase of the atoms within a central region of length $l_h$ = 6 nm, while keeping 10 atomic layers at both ends of each NW at room temperature. This prescribed temperature profile is imposed by applying a Langevin thermostat[52] only to the atoms in the heated region and in the cold boundary layers (yellow and purple atoms in Fig. 1). Periodic boundary conditions are enforced at the NW ends, whereas the nanowires are free to expand or contract radially. All other atoms are not directly thermostatted by Langevin and evolve under the system-level dynamics. The equations of motion are integrated in the NPT ensemble using a Nosé–Hoover thermostat and barostat.[22,41]

The simulation of the welding process consists of three stages: heating, holding, and cooling. During the heating stage the temperature is brought from room temperature to a target value corresponding to either $0.3T_m$, $0.6T_m$ or $0.85T_m$, being $T_m$ = 962 °C for Ag. This stage lasts for 0.9 ns with a time step of 0.002 ps to ensure a controlled and progressive temperature increase, such that the system converges to the prescribed $T_{target}$ by the end of the heating phase. The final junction nanostructure and the interpenetration factor IF are primarily governed by the holding stage at $T_{target}$, which is held constant until IF reaches a plateau. At $0.3T_m$ and $0.6T_m$, the holding stage ends at equilibrium, determined using a convergence criterion (for details see section 1 of the SI), which is found to occur after 47.9 ns and 75.9 ns, respectively. However, to maintain consistency and facilitate a comparison of results, the simulations at $0.3T_m$ are extended to match the convergence time of those at $0.6T_m$. At $0.85T_m$, the stage is manually stopped at 75.9 ns to prevent Rayleigh instability, ensuring full NW interpenetration as discussed in section 3.

During the holding phase at $T_{target}$, the time step is set to 0.015 ps, the maximum value deemed reliable for our simulations. Exceeding this threshold results in unstable particle motion due to significant truncation errors in the integration process, leading to a critical increase in the total energy of the system.[13,31] The cooling stage follows, during which the thermostat target temperature is set to room temperature and the system is allowed to cool down freely in the NPT ensemble. The cooling time is not imposed *a priori* and varies depending on the target temperature at which sintering occurred. After cooling, the system is kept at room temperature in the NPT ensemble for the remaining time, such that the overall post-welding time (cooling plus relaxation) is 1.0 ns. For these phases, the time step is set to 0.002 ps. The cooling stage and subsequent relaxation are introduced to progressively remove thermal fluctuations and avoid quenching-induced artifacts. Their total duration is selected to ensure a sufficiently gradual temperature decrease, thereby minimizing the influence of the post-welding cooling on the resulting nanowire junction nanostructure. Additional details on the preliminary procedures required for nanowire construction and junction assembly are provided in section 2 of the SI.

The interaction between atoms is described through the embedded-atom method (EAM). The potential formulated by Williams *et al.*[60] is applied to model the interactions among silver atoms. The simulations are performed using the GPU package[4] of the Large-scale Atomistic/Molecular Massively Parallel Simulator (LAMMPS).[47] The simulated structures are visualized by means of the Open Visualization Tool (OVITO).[56]

## 3 Welding NWs with generic orientations across target temperatures

This section aims to provide an initial assessment of interpenetration and nanostructural changes in nanowires subject to different target temperatures, while also contrasting the behavior of SC and PT nanowires. To this end, two generic orientations of the nanowires are considered, namely $\theta_1 = 0°$, $\theta_2 = 35°$ for SC and $\theta_1 = 0°$, $\theta_2 = 18°$ for PT, and three target temperatures: $0.3T_m$, $0.6T_m$, and $0.85T_m$. The variation of the interpenetration factor during the welding process is presented in Fig. 2(a) for both types of NWs. The nanostructure of the junction obtained at the end of the simulation is shown in Fig. 2(b), where the target temperature increases from the left to the right panel. The images show the cross-section of the nanojunction, sliced in half by the *xz* plane. The atoms are colored according to the Common Neighbor Analysis (CNA):[11,21] green atoms represent an FCC configuration, red atoms indicate an HCP configuration while gray atoms do not belong to any of the recognized crystalline structures included in the CNA classification.

Three main observations can be made: (1) higher target temperatures result in greater interpenetration for both types of nanowires (SC and PT); (2) at all temperatures, PT nanowires exhibit a larger interpenetration factor compared to SC nanowires; (3) higher target temperatures lead to more pronounced nanostructural changes at the junction.

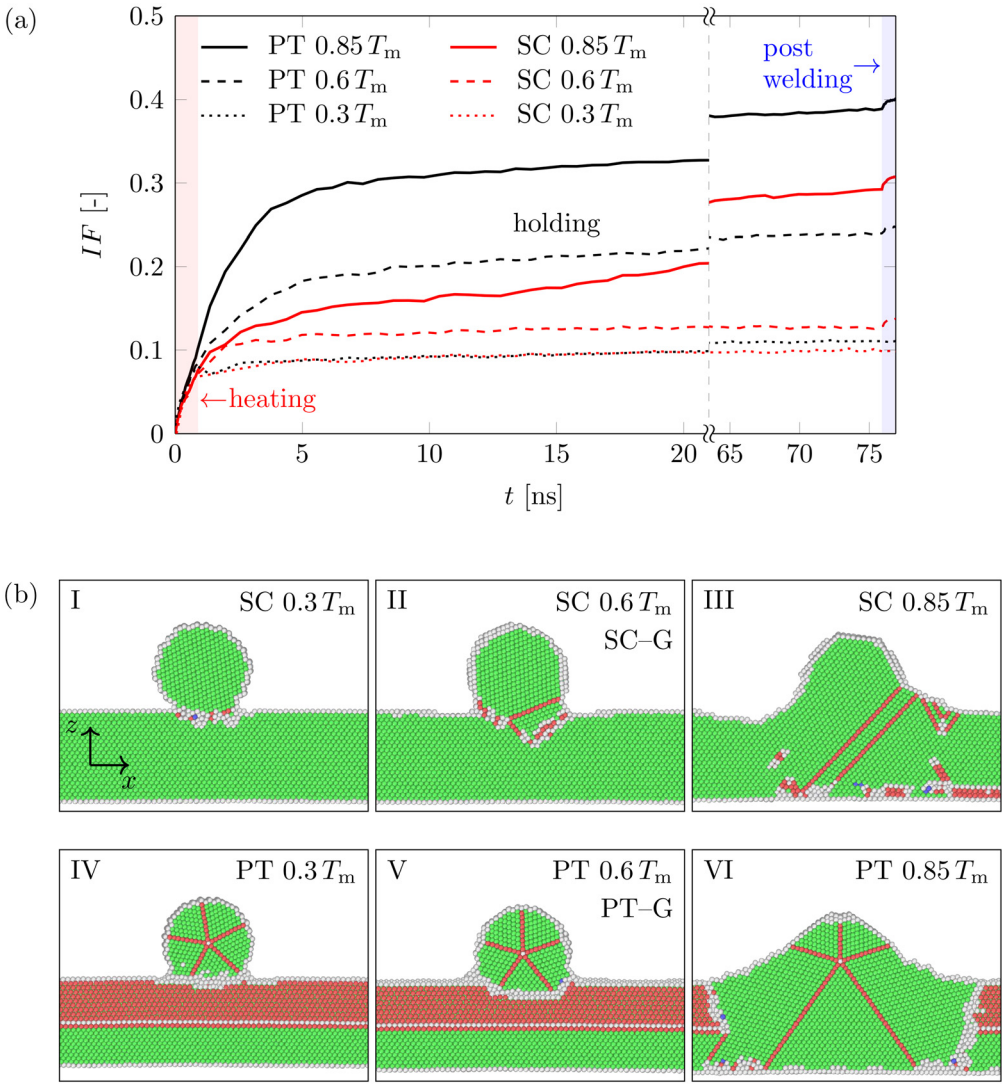


**Fig. 2** Effect of the target temperature. (a) Evolution of the interpenetration factor IF during the welding process at various target temperatures $T_{target}/T_m \in \{0.3, 0.6, 0.85\}$. The time intervals corresponding to the heating stage and the post-welding stage (cooling followed by relaxation at room temperature) are highlighted in red and blue, respectively. Part of the data corresponding to the holding stage is omitted for the sake of readability. (b) Cross-sectional views of the modeled junctions at the end of the post-welding stage. The atoms are colored according to the common neighbor analysis: green atoms represent an FCC configuration, red atoms indicate an HCP configuration while gray atoms do not belong to any of the recognized crystalline structures included in the CNA classification.

When the junction is formed at $0.3T_m$, both types of nanowires exhibit minimal interpenetration and maintain their original nanostructure after welding; the connection occurs through a grain boundary, since NWs in generic orientations do not present the same crystallographic plane either in the *xy* or in the *yz* section of the weld. When the target temperature is $0.6T_m$, the nanowires exhibit greater interpenetration, connecting through a grain boundary and showing minor nanostructural changes, such as a few defects at the connection between SC NWs and a slight growth of one of the upper twin boundaries for the PT pair. These junctions closely resemble those observed in experimental results reported in the literature, as they display significant interpenetration with negligible structural changes. Park *et al.*[44] observed a similar configuration in their experiments, where fast Fourier transform patterns of the junction revealed two orientations corresponding to the original NWs, confirming that the two NWs remained crystallographically distinct.[24]

The top nanowire fully grows into the bottom one only at a target temperature of $0.85T_m$. This is evident in the case of the PT NW junction in the bottom right panel of the figure. The growth of one wire into the other was also observed experimentally by Garnett *et al.*,[15] who reported that, after the plasmonic welding process, a single orientation was present after illumination of the junction, suggesting the complete growth of one NW into the other.

For the numerical simulations conducted at $0.3T_m$ and $0.6T_m$, the holding stage is terminated once the system reaches equilibrium at the target temperature $T_{target}$, determined using a convergence criterion based on IF, as detailed in section 1 of the SI. Equilibrium is achieved more rapidly in simulations performed at $0.3T_m$. However, to ensure a consistent and structured presentation of results, these simulations are extended to match the convergence time of the $0.6T_m$ simulations, which is 75.9 ns.

For the higher target temperature, the simulations indicate a significant increase of interpenetration during holding for both nanowire types. In fact, the nanostructure obtained at the end of the process would further evolve if one would permit longer times. We have stopped the simulation because at longer times (or higher temperatures), owing to the high diffusion rate, the nanowires would become very thin close to the junction and finally break due to the Rayleigh instability.[7,36,45,58]

The welding process, at the temperatures considered in this study, does not involve melting and solidification but is similar to a sintering process without applied pressure: the driving mechanism is heat-induced atomic diffusion.

Atomic diffusion is driven by the reduction of the total surface energy of the system. In particular, according to the Gibbs–Thomson effect, surface regions characterized by higher curvature (*i.e.*, smaller radius of curvature) exhibit a higher chemical potential. This provides a thermodynamic driving force for atomic transport from highly curved regions toward flatter ones, promoting neck growth and reducing the overall surface area, consistently with classical solid-state sintering mechanisms.

Even when two identical Ag nanowires are brought into contact, the contact geometry creates a strong surface-curvature contrast around the incipient neck; diffusion is therefore driven by surface free-energy minimization (Gibbs–Thomson effect) despite the absence of any chemical or compositional gradients.

While curvature provides the thermodynamic driving force, diffusion kinetics are strongly dependent on crystallography as discussed in section 2.1. This orientation-dependent mobility explains why different junction configurations exhibit markedly different interpenetration factors, even under identical thermal conditions, as shown in Fig. 2(a). A systematic comparison across junction types is presented in section 4.2 and illustrated in Fig. 7.

To conclude, the simulations show that a target temperature of $T_{target} = 0.6T_m$ is sufficiently high to ensure that the atomistic reorganization process observed in the experiments is triggered, resulting in a final nanostructure where the NWs are well-connected yet remain distinguishable.[44] Furthermore, at $0.6T_m$ the process is more easily controllable than at $0.85T_m$, since the junction reaches its final nanostructure gradually during the holding stage, and there is no risk of premature breaking due to Rayleigh instability. Moreover, the junction obtained at higher temperature is more prone to failure during use, as diffusion leaves thinned vulnerable wires next to a thick, highly resistant junction (as widely reported by experimental studies in literature[6,7,15,27]). For this reason we will consider in the rest of the manuscript only the intermediate target temperature $0.6T_m$. The two configurations identified in this section are retained for subsequent use throughout the manuscript and are hereafter denoted as SC–G and PT–G as indicated in Fig. 2. As a disclaimer, it is important to stress that temperatures and times in atomistic simulations are not directly transferable to experiments.

# 4 Effect of crystalline orientation

To establish the upper and lower bounds of interpenetration and, at the same time, gain insight into variations in junction nanostructure, it is critical to consider notable orientations. Considering the whole spectrum of possible nanostructures is relevant because the nanostructure controls the electrical and mechanical responses of the individual junction; moreover, inhomogeneities in the nanostructures might affect the percolation network and thus the global behavior of the device.[17,18,51]

## 4.1 Notable orientations

Three configurations, illustrated in Fig. 3 and 5, are considered for the PT and SC NW pairs. The various orientations are obtained by rotating the nanowires around their longitudinal axes by $\theta_1$ and $\theta_2$ (Fig. 1). The starting configuration for the PT nanowires, $\theta_1 = \theta_2 = 0$, is taken such that the center of the "faces" of two twin sectors are in contact; this is referred to as the PT–FF configuration, where "face" denotes the surface region of the cylindrical sector between two twin boundaries as shown in Fig. 4.

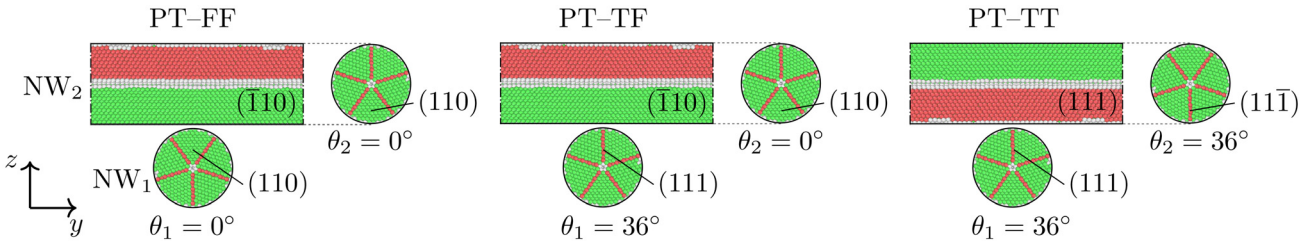


**Fig. 3** Various PT nanowire configurations prior to welding: on the left-hand side, top and bottom NW are touching face-to-face (PT–FF), in the middle, twin-to-face (PT–TF), and on the right-hand side, twin-to-twin (PT–TT). Angles $\theta_1$ and $\theta_2$, defined in Fig. 1, specify the orientations of the nanowires relative to the reference PT–FF configuration.

In the second configuration, $\theta_1 = 36°$ and $\theta_2 = 0°$, a twin plane of $NW_1$ touches a face of $NW_2$ and is thus referred to as PT–TF. The third configuration, $\theta_1 = \theta_2 = 36°$, has two twin planes in contact and is referred to as PT–TT.

These notable configurations are referred to as PT–FF, PT–TF, and PT–TT, and they encompass all distinct junction types that arise from symmetry considerations (Table 1). The origin of these configurations can be understood by examining the fivefold symmetry of the PT nanowire cross-section, which consists of five isosceles triangular sectors with vertex angle 36°. As a result, the set of representative junction configurations reduces to three distinct configurations: PT–FF (corresponding to contact between two faces), PT–TF (describing the interaction between a twinned plane and the "center" of a face), and PT–TT (corresponding to contact between two twinned planes), as shown in Fig. S3 in the SI.

For completeness, we also consider a generic configuration denoted PT–G, corresponding to a relative misorientation of 18° from PT–FF, which is used as a representative generic misorientation. During welding, we observe a rigid rotation of the top nanowire that progressively reduces this misorientation, such that the resulting junction nanostructure becomes similar to that of PT–TF. It should be noted, however, that although the final junction nanostructure is similar for configurations with initial misorientations between 0° and 18°, the interpenetration factor IF remains dependent on the extent of the rotation undergone by the nanowire.

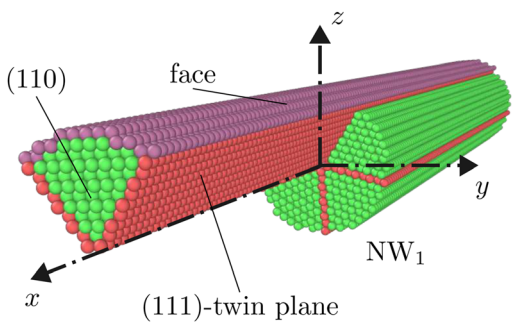


**Fig. 4** Penta-twinned NW structure. Purple atoms highlight the surface region of the cylindrical sector between two twin boundaries, which we refer to as the "face".

**Table 1** Nomenclature and classification of junction types used in this study

| | Cross section | Label | Junction description |
|---|---|---|---|
| Penta-twinned | Circular | PT–FF | Face-to-face |
| | | PT–TF | Twin-to-face |
| | | PT–G | Twin-to-face (generic misorientation, off-centered) |
| | | PT–TT | Twin-to-twin |
| | Pentagonal | PT–SS | Side-to-side |
| | | PT–VS | Vertex-to-side |
| | | PT–VV | Vertex-to-vertex |
| Single crystal | Circular | SC 0–0 | (110)-to-(110) |
| | | SC–G | Generic misorientation |
| | | SC 90–90 | (001)-to-(110) |
| | | SC 35–35 | (111)-to-(110) |
| | Pentagonal | SC–SS | Side-to-side |
| | | SC–VS | Vertex-to-side |
| | | SC–VV | Vertex-to-vertex |

The configurations of the SC NWs are instead selected such as to align specific crystallographic orientations. As all NWs are grown in the ⟨110⟩ direction, their cross-sectional areas correspond to (110) planes. Rotations of the nanowires about their longitudinal axes permit to join different crystallographic planes, as illustrated in Fig. 5. The first configuration corresponds to $\theta_1 = \theta_2 = 0$, is named SC 0–0, and the *yz* cross-section of the junction lies in both nanowires on a (110) plane, while the *xy* cross-section lies on a (001) plane. In the second configuration, SC 90–90, with $\theta_1 = \theta_2 = 90°$, the *xy* cross-section of the junctions lies on the (1̄10) planes, while the *yz* section cuts the (001) planes of the top nanowire and the (110) plane of the bottom one. For the third configuration, SC 35–35, the *xy* cross-section of the junction lies on the (2̄11) plane and cuts the top nanowire along the (111) plane and the bottom nanowire along the (110) plane.

The nanojunctions obtained after welding at the target temperature of $0.6T_m$ are presented in Fig. 6. For comparison, the junctions with generic orientations previously obtained at $0.6T_m$ (section 3) are also included. These are labeled as PT–G and SC–G (formerly PT $0.6T_m$ and SC $0.6T_m$; see Fig. 2). From these results, three main observations can be drawn.

(1) When the crystallographic planes lying on the *yz* section are both (110) (case SC 0–0 or PT–FF), a commensurate interface forms without a grain boundary. In all other cases, a grain

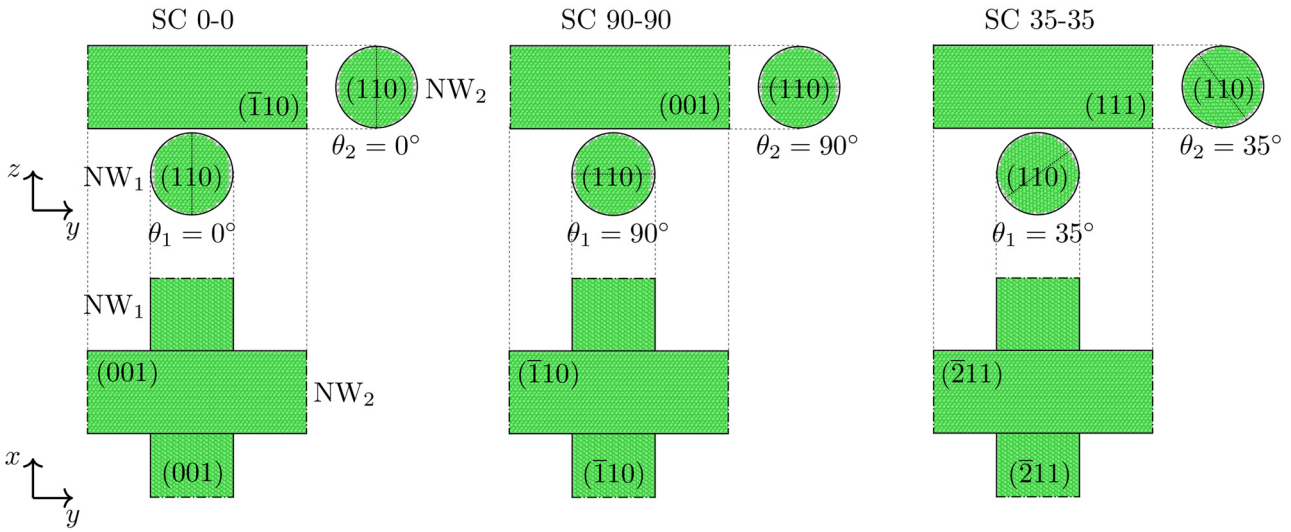


**Fig. 5** Specific configurations for the SC NWs: on the left-hand side, the SC 0–0 configuration has both wires disposed such that the (110) planes lie on *yz* sections while (001) planes lie on *xy* sections; in the middle configuration, SC 90–90, the *xy* section cuts both wires along $(\bar{1}10)$ planes, while the *yz* section cuts the top wire along (001) planes and the bottom nanowire along the (110) plane; on the right hand side, the NWs in the SC 35–35 configuration are cut by *xy* planes on the $(\bar{2}11)$ planes, while the *yz* plane cuts the top nanowire along a (111) plane and the bottom along a (110) plane.

boundary and other defects, such as stacking faults and/or dislocations, are present around the weld.

(2) The degree of interpenetration depends on the initial orientation of the nanowires, as atomic diffusion is strongly influenced by this orientation.

(3) For PT nanowires, the top nanowire can undergo a rigid rotation about its longitudinal axis during welding. This rotation is configuration-dependent, as shown in Fig. S4 in the SI, which reports the evolution of the rigid rotation angle. The rotation is negligible for PT–FF and PT–TF (panels IV and V in Fig. 6), whereas it becomes significant for PT–G (panel V in Fig. 2) and PT–TT (panel VI in Fig. 6), reaching approximately 20° and 34°, respectively. These rotations are mainly driven by the presence of twin boundaries: the top nanowire adjusts its orientation to reduce the initial misorientation and prevent its twin planes from being obstructed by those of the bottom nanowire during interpenetration. This progressive reorientation drives the junction nanostructure toward a similar twin-to-face contact geometry, close to PT–TF. In actual networks, however, such rotations are expected to be restricted because nanowires are connected to multiple junctions simultaneously, suggesting that our results represent upper bounds.

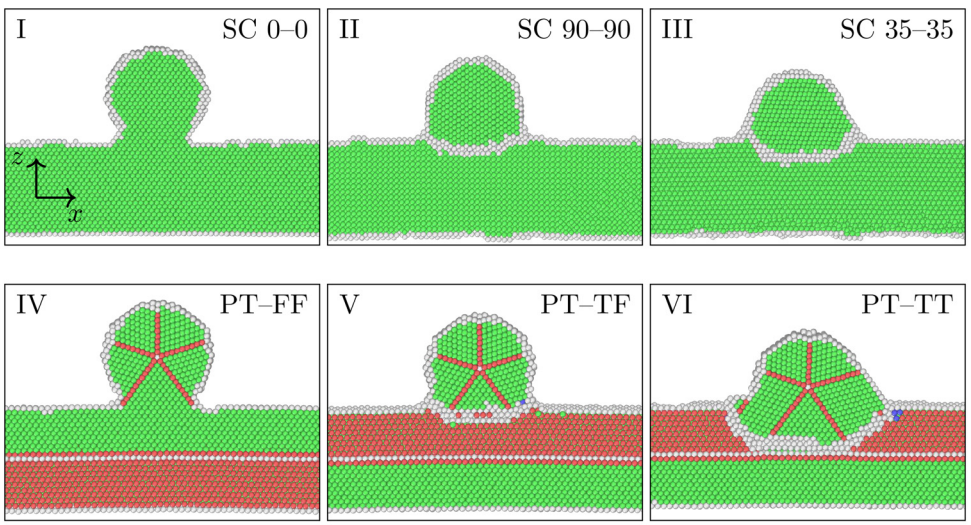


**Fig. 6** Effect of the relative orientation of the crystalline structure of NWs on the resulting junction. Cross-sectional views at the center of the junction by the *yz* plane. The panels show the nanostructure of the junction at the end of the post-welding stage.

### 4.2 Interpenetration of notable and generic orientations

The final values of IF for all configurations studied so far are compiled in Fig. 7. The lower bound value, IF = 0.04, is the same for SC and PT nanowires and is achieved when the atomic spacing is commensurate and the grain boundary does not form. Note that these junctions are not necessarily worse than the others from an electrical and mechanical viewpoint, as the absence of defects delays plasticity and does not impair electrical conductance.

The PT NWs span a broader range in IF values, with the upper bound, IF = 0.38, reached by the PT–TT configuration. Note also that, in generic orientation, PT nanowelds achieve greater interpenetration than their SC counterparts. Since the spectrum of generic orientations is much wider than that of the notable ones, we conclude that the interpenetration of PT nanowelds is generally larger than that of SC nanowelds. The results provide a complete picture of the possible interpenetrations of nanowires, since intermediate cases all fall within the range reported here, with interpenetration values more likely to cluster around the SC–G and PT–G cases.

The data reported in Fig. 7 have been sampled after convergence, by measuring the interpenetration of nanowires held for 75.9 ns at $0.6T_m$, as shown in Fig. S5 in the SI. The plateaus in the curves in Fig. S5 confirm that this holding time is sufficient. Further, the ordering PT–TT > PT–G > PT–TF > PT–FF underscores the role of twin-plane involvement at the contact: interpenetration increases from face-to-face contact (PT–FF), to twin-plane–face contact (PT–TF and PT–G), to twin-to-twin contact (PT–TT). Note that both PT–TF and PT–G involve one twin plane contacting a face: in PT–TF the twin plane is aligned with the face center, whereas in PT–G it is laterally offset (generic misorientation), which results in a different interpenetration level.

### 4.3 The role of surface curvature and twin boundaries

Experimental micrographs reveal significant variability in the geometry, shape, and resulting nanostructure of junctions within NW networks.[6,7,44] This variation arises from differences in the original shapes and dimensions of the nanowires, which also affect the welding conditions. For instance, nanowire diameters can differ by up to 50 nm,[15] leading to variations in the thermal energy required for sintering each junction. Also, the cross-section of penta-twinned nanowires can be either circular or pentagonal with slightly rounded corners, allowing the range of surface curvatures within the nanowire network to vary widely. As surface diffusion depends on curvature, the curvature of each nanowire in the junction will contribute to the final interpenetration and overall nanostructure.

Experimental work reported by Radmilović *et al.*[49] shows that the formation of a junction between PT AgNWs pairs with pentagonal cross-sections is promoted when the contact involves a facet and a vertex but is hindered when the contact occurs solely at facets. In these pentagonal nanowires, the vertices correspond to twin planes. The enhanced welding observed at the vertices was attributed to the role of curvature, as increased curvature was shown to promote diffusion. In our previous simulations (section 4.1), we employed circular cross-sections, thereby eliminating the influence of curvature as a variable. This allowed us to focus solely on the effect of twin boundaries. Our results show that configurations involving twin planes (PT–TT, PT–TF, PT–G) exhibited significantly deeper interpenetration compared to those without twin plane involvement (PT–FF).

These findings raise a critical question: is the observed interpenetration—and consequently the enhanced diffusion—primarily driven by the presence of twin boundaries, by curvature, or by an interplay of both factors? To address this question, we replicate several simulations from section 4.1 using both PT and SC nanowires with pentagonal cross-sections. These cross-sections are defined as the largest pentagon inscribed within a circle of diameter $d_w$ = 5.4 nm. This specific diameter is chosen to minimize surface roughness along the pentagon's edges while ensuring that the nanowires contain the same number of atoms as those with circular cross-sections.

Three orientations are considered for both SC and PT nanowires: side-to-side, where the nanowires touch at their flat facets; vertex-to-side, where the junction involves the flat facet of one nanowire and the vertex of the other; and vertex-to-vertex, where both nanowires touch each other at their tips. These configurations are denoted as SS, VS, and VV, respectively.

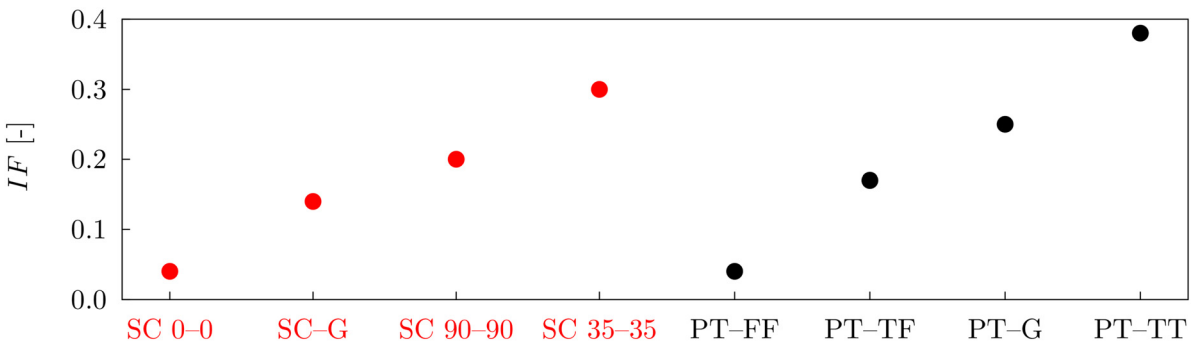


**Fig. 7** Final IF for notable and generic configurations, the latter are named SC–G and PT–G. The data points for the single crystals are in red, for the penta-twinned nanowires in black.

We start by simulating SC nanowires with pentagonal cross-sections, maintaining the same structural and crystallographic orientation as the SC 0–0 wires. Although this geometry has not been reported in the literature and is not observed during typical synthesis processes, it was included in our study as an ideal case that can be directly contrasted to the PT nanowire with identical shape to assess the effect of the twin boundaries.

At the end of the post-welding stage, the IF values for the SC–SS, SC–VS, and SC–VV configurations reached 0.02, 0.08, and 0.12, respectively as shown in Fig. 8. The vertex-to-vertex (SC–VV) and vertex-to-side (SC–VS) nanojunctions exhibited interpenetration values that were 3 and 2 times greater, respectively, than those observed in the circular SC 0–0 configuration. In contrast, side-to-side nanojunctions (SC–SS) resulted in half of the interpenetration observed in the SC 0–0 configuration. The results are in agreement with the description by Radmilović *et al.*[49]: higher curvature (smaller radius of curvature) induces greater interpenetration, even in SC, *i.e.*, when twin planes are absent.

We then extended our simulations to PT nanowires with pentagonal cross-sections. At the end of the post-welding stage, the IF values reached 0.02 for PT–SS, 0.21 for PT–VS, and 0.48 for PT–VV, as shown in Fig. 8. Notably, the interpenetration in the vertex-to-vertex nanojunctions (PT–VV) is 1.26 times higher than that in the circular PT–TT configuration and 2.82 times higher than PT–TF. In contrast, the side-to-side nanojunctions (PT–SS) exhibited half the interpenetration of the circular PT–FF. Table 2 lists the interpenetration factor values for all configurations considered in this study.

The atomistic configurations after the post-welding stage indicate outcomes similar to those observed for their circular-section counterparts, as reported in Fig. S6 in the SI. Junctions formed by SC NWs consistently exhibit a commensurate interface without grain boundaries, irrespective of the configuration (SC–SS, SC–VS, and SC–VV). For PT NWs, the PT–SS configuration results in a continuous and regular pattern across the junction. In contrast, the PT–VS and PT–VV configurations undergo structural rearrangements similar to those observed in their circular-section counterparts. Furthermore, the PT–VV configuration exhibits a rotation of the top nanowire about its longitudinal axis of approximately 30°, closely aligned with the rotation observed in the PT–TT configuration.

These simulation results confirm the findings of Radmilović *et al.*[49] and extend them by demonstrating that the impact of curvature on interpenetration varies with the nanowire structure. For SC nanowires, higher curvature enhances interpenetration by an average factor of 2.5, computed as the mean of the ratios $IF_{SC-VS}/IF_{SC\ 0-0} = 0.08/0.04 = 2$ and $IF_{SC-VV}/IF_{SC\ 0-0} = 0.08/0.04 = 3$. For PT nanowires, the increase is more modest, at approximately 1.25, computed as the mean of $IF_{PT-VS}/IF_{PT-TF} = 0.21/0.17 = 1.24$ and $IF_{PT-VV}/IF_{PT-TT} = 0.48/0.38 = 1.26$, *i.e.*, using as reference the closest circular configurations with the same type of twin-plane involvement.

Consequently, we conclude that curvature plays a dominant role in determining the depth of the junction in SC nanowires, whereas for PT nanowires, the relative orientation of the crystalline structures is the primary factor influencing the structure and depth of the resulting junction. The effect of twin boundaries is more pronounced than that of curvature in

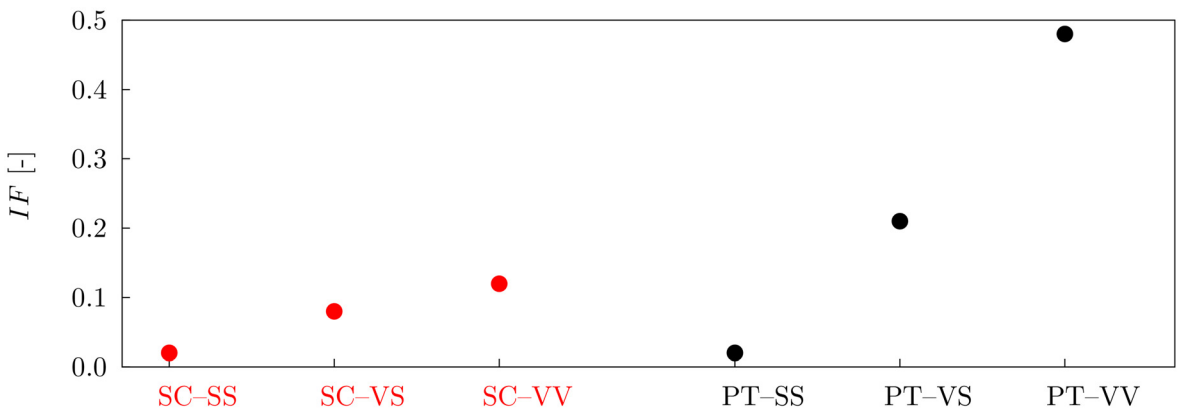


**Fig. 8** Final IF for SC (in red) and PT (in black) nanowires with pentagonal cross-section.

**Table 2** Interpenetration factor values for each junction type

| Penta-twinned (PT) | FF | TF | G | TT | SS | VS | VV |
|---|---|---|---|---|---|---|---|
| IF | 0.04 | 0.17 | 0.25 | 0.38 | 0.02 | 0.21 | 0.48 |
| Single crystal (SC) | 0–0 | G | 90–90 | 35–35 | SS | VS | VV |
| IF | 0.04 | 0.14 | 0.20 | 0.30 | 0.02 | 0.08 | 0.12 |

influencing variations in the nanostructure of the nanowires at the junction.

## 5 Discussion and final remarks

Our atomistic simulations provide indirect indicators linking to the mechanical and electrical performance of nanowire junctions, as discussed below.

In general, a larger interpenetration factor IF corresponds to a larger neck, which usually improves electrical and mechanical connectivity. An exception occurs in commensurate SC interfaces (*e.g.*, SC 0–0 in Fig. 7). Here the IF is small, yet the two lattices are perfectly aligned across the junction, with no grain boundary. This atomic continuity could ensure low contact resistance and enhance mechanical stability, even though the visible overlap is limited. This observation underscores that interpenetration alone does not fully describe junction quality and should be interpreted together with the defect content of the welded region. The simulations reveal the presence of defects within the junctions, mostly in the form of irregular grain boundaries and dislocations, which correspond to regions where the electrical and mechanical responses are expected to be inhomogeneous. Electrically, defects are known to scatter electrons and increase resistance; mechanically, they might act as nucleation sites for plastic deformation or crack initiation.

For PT nanowires, an additional mechanism contributes to junction evolution. Junctions involving twin planes in PT nanowires (PT–TF and PT–TT) show deeper interpenetration (Fig. 7). During welding, the upper nanowire may undergo a rigid rotation to align its twin planes with those of the lower one, reducing obstruction and promoting further penetration (Fig. S4 in the SI). This configuration-dependent rotation provides a pathway toward a more favorable local twin-to-face contact geometry and therefore contributes to the larger interpenetration observed in PT junctions.

In real networks, however, such rotations are often restricted because wires are connected to several junctions at once. This limitation prevents misalignments from being relaxed, leading to local stress build-up and increased variability in junction quality. Overall, these observations suggest that commensurate SC junctions can provide low resistance and mechanical robustness despite their limited overlap, while PT junctions achieve larger interpenetration but also exhibit wider variability. For PT networks, controlling orientation or restricting unwanted rotations may improve both electrical and mechanical reliability.

Overall, our simulations identify the upper and lower bounds of interpenetration achievable when forming junctions between SC and PT nanowires at a temperature that promotes sintering without inducing melting or major disruption of the original nanowire nanostructure. The resulting junction nanostructure and interpenetration depend strongly on the nanowire internal structure (SC *versus* PT), and simulations restricted to single-crystal nanowires are therefore not representative of the broader behavior of penta-twinned nanowires.[7,24,39] In addition, the relative crystallographic orientation prior to welding plays a decisive role, implying that single-configuration studies cannot capture the variability expected in realistic networks. While the lower bound of IF is similar for SC and PT nanowires, PT junctions exhibit a higher upper bound and therefore a broader variability, which is expected to translate into a wider distribution of junction qualities in PT-based networks. Finally, comparing circular and pentagonal cross-sections confirms that, although surface curvature contributes to diffusion-driven interpenetration, the presence and arrangement of twin boundaries in PT nanowires play the dominant role in promoting nanostructural evolution during welding.

## Author contributions

Matteo Ferliga: conceptualization, data curation, formal analysis, investigation, methodology, software, writing – original draft. Davide Grazioli: conceptualization, investigation, writing – review & editing. Angelo Simone: conceptualization, funding acquisition, supervision, writing – review & editing. Lucia Nicola: conceptualization, funding acquisition, project administration, supervision, writing – review & editing.

## Conflicts of interest

There are no conflicts to declare.

## Data availability

Data for this article are available at Zenodo at https://doi.org/10.5281/zenodo.17432648.

Supplementary information (SI) cites additional references[3,8,14,20,40,49,53] that are included in the reference list.

Supplementary information is available. See DOI: https://doi.org/10.1039/d5nr04486c.

## Acknowledgements

L. N. acknowledges funding from the Department of Industrial Engineering at the University of Padova for the project From metal-nanojunctions to flexible electronics: A dual-scale numerical approach (Finanziamento SID 2023). A. S. acknowledges funding from the Department of Industrial Engineering at the University of Padova for the project Computational multiscale and multiphysics modeling of mechanically induced failure in fibrous metal transparent flexible electrodes (Finanziamento SID 2022).

Use of AI tools declaration: a generative AI language model was used to assist with improving the readability and language of this manuscript. The authors reviewed and edited all content and take full responsibility for the final version of the publication.

## References


1 F. Baletto, C. Mottet and R. Ferrando, Molecular dynamics simulations of surface diffusion and growth on silver and gold clusters, *Surf. Sci.*, 2000, **446**(1–2), 31–45.

2 J. Bang, S. Coskun, K. R. Pyun, D. Doganay, S. Tunca, S. Koylan, D. Kim, H. E. Unalan and S. H. Ko, Advances in protective layer-coating on metal nanowires with enhanced stability and their applications, *Appl. Mater. Today*, 2021, **22**, 100909.

3 E. Bitzek, P. Koskinen, F. Gähler, M. Moseler and P. Gumbsch, Structural relaxation made simple, *Phys. Rev. Lett.*, 2006, **97**(17), 170201.

4 W. M. Brown, P. Wang, S. J. Plimpton and A. N. Tharrington, Implementing molecular dynamics on hybrid high performance computers–short range forces, *Comput. Phys. Commun.*, 2011, **182**(4), 898–911.

5 T. Chen, H. Peng, M. Durstock and L. Dai, High-performance transparent and stretchable all-solid supercapacitors based on highly aligned carbon nanotube sheets, *Sci. Rep.*, 2014, **4**(1), 3612.

6 W.-H. Chung, Y.-R. Jang, Y.-T. Hwang, S.-H. Kim and H.-S. Kim, The surface plasmonic welding of silver nanowires via intense pulsed light irradiation combined with NIR for flexible transparent conductive films, *Nanoscale*, 2020, **12**(34), 17725–17737.

7 J. Cui, X. Ren, X. Mei, Z. Fan, C. Huang, Z. Wang, X. Sun and W. Wang, Morphological characteristics and atomic evolution behavior of nanojoints in Ag nanowire interconnect network, *Int. J. Extreme Manuf.*, 2023, **5**(2), 025503.

8 R. De Wit, Partial disclinations, *J. Phys. C: Solid State Phys.*, 1972, **5**(5), 529.

9 H. Devaraj, Q. Tian, W. Guo and R. Malhotra, Multiscale modeling of sintering-driven conductivity in large nanowire ensembles, *ACS Appl. Mater. Interfaces*, 2021, **13**(47), 56645–56654.

10 Y. Ding, Y. Cui, X. Liu, G. Liu and F. Shan, Welded silver nanowire networks as high-performance transparent conductive electrodes: Welding techniques and device applications, *Appl. Mater. Today*, 2020, **20**, 100634.

11 D. Faken and H. Jónsson, Systematic analysis of local atomic structure combined with 3D computer graphics, *Comput. Mater. Sci.*, 1994, **2**(2), 279–286.

12 F.-R. Fan, L. Lin, G. Zhu, W. Wu, R. Zhang and Z. L. Wang, Transparent triboelectric nanogenerators and self-powered pressure sensors based on micropatterned plastic films, *Nano Lett.*, 2012, **12**(6), 3109–3114.

13 D. Fincham, Choice of timestep in molecular dynamics simulation, *Comput. Phys. Commun.*, 1986, **40**(2–3), 263–269.

14 Y. Gao, L. Song, P. Jiang, L. Liu, X. Yan, Z. Zhou, D. Liu, J. Wang, H. Yuan, Z. Zhang, X. Zhao, X. Dou, W. Zhou, G. Wang, S. Xie, H. Chen and J. Li, Silver nanowires with five-fold symmetric cross-section, *J. Cryst. Growth*, 2005, **276**(3–4), 606–612.

15 E. C. Garnett, W. Cai, J. J. Cha, F. Mahmood, S. T. Connor, M. G. Christoforo, Y. Cui, M. D. McGehee and M. L. Brongersma, Self-limited plasmonic welding of silver nanowire junctions, *Nat. Mater.*, 2012, **11**(3), 241–249.

16 W. Gaynor, G. F. Burkhard, M. D. McGehee and P. Peumans, Smooth nanowire/polymer composite transparent electrodes, *Adv. Mater.*, 2011, **23**(26), 2905–2910.

17 D. Grazioli, A. C. Dadduzio, M. Roso and A. Simone, Quantitative electrical homogeneity assessment of nanowire transparent electrodes, *Nanoscale*, 2023, **15**(14), 6770–6784.

18 D. Grazioli, G. Gangi, L. Nicola and A. Simone, Predicting mechanical and electrical failure of nanowire networks in flexible transparent electrodes, *Compos. Sci. Technol.*, 2024, **245**, 110304.

19 D. Grazioli, L. Nicola and A. Simone, Debunking misconceptions about cross-aligned nanowire network electrodes, *Nanotechnology*, 2025, **36**(25), 255204.

20 J. Guénolé, W. G. Nöhring, A. Vaid, F. Houllé, Z. Xie, A. Prakash and E. Bitzek, Assessment and optimization of the fast inertial relaxation engine (fire) for energy minimization in atomistic simulations and its implementation in LAMMPS, *Comput. Mater. Sci.*, 2020, **175**, 109584.

21 J. D. Honeycutt and H. C. Andersen, Molecular dynamics study of melting and freezing of small Lennard-Jones clusters, *J. Phys. Chem.*, 1987, **91**(19), 4950–4963.

22 W. G. Hoover, Canonical dynamics: Equilibrium phase-space distributions, *Phys. Rev. A*, 1985, **31**(3), 1695.

23 L. Hu, D. Hecht and G. Grüner, Percolation in transparent and conducting carbon nanotube networks, *Nano Lett.*, 2004, **4**(12), 2513–2517.

24 Y. Hu, X. Zhang, H. Ding and Y. Hu, Laser shock-enabled optical–thermal–mechanical coupled welding method for silver nanowires, *Int. J. Mach. Tools Manuf.*, 2024, **199**, 104162.

25 Q. Huang and Y. Zhu, Gravure printing of water-based silver nanowire ink on plastic substrate for flexible electronics, *Sci. Rep.*, 2018, **8**(1), 15167.

26 M. N. Jahangir, H. Devaraj and R. Malhotra, On self-limiting rotation and diffusion mechanisms during sintering of silver nanowires, *J. Phys. Chem. C*, 2020, **124**(36), 19849–19857.

27 Y.-R. Jang, W.-H. Chung, Y.-T. Hwang, H.-J. Hwang, S.-H. Kim and H.-S. Kim, Selective wavelength plasmonic flash light welding of silver nanowires for transparent electrodes with high conductivity, *ACS Appl. Mater. Interfaces*, 2018, **10**(28), 24099–24107.

28 J. Jiang, S. Chu, Y. Zhang, G. Sun, J. Jin, X. Zeng, M. Chen and P. Liu, Crystal plane orientation-dependent surface atom diffusion in sub–10 nm Au nanocrystals, *Sci. Adv.*, 2024, **10**(21), eadn5946.

29 H. Y. Jung, M. B. Karimi, M. G. Hahm, P. M. Ajayan and Y. J. Jung, Transparent, flexible supercapacitors from nano-engineered carbon films, *Sci. Rep.*, 2012, **2**(1), 773.

30 H. Khaligh, L. Xu, A. Khosropour, A. Madeira, M. Romano, C. Pradére, M. Tréguer-Delapierre, L. Servant, M. A. Pope and I. A. Goldthorpe, The Joule heating problem in silver nanowire transparent electrodes, *Nanotechnology*, 2017, **28**(42), 425703.

31 S. Kim, Issues on the choice of a proper time step in molecular dynamics, *Phys. Procedia*, 2014, **53**, 60–62.
32 S. Lee, J. Jang, T. Park, Y. M. Park, J. S. Park, Y.-K. Kim, H.-K. Lee, E.-C. Jeon, D.-K. Lee, B. Ahn and C.-H. Chung, Electrodeposited silver nanowire transparent conducting electrodes for thin-film solar cells, *ACS Appl. Mater. Interfaces*, 2020, **12**(5), 6169–6175.
33 S. Lin, H. Wang, X. Zhang, D. Wang, D. Zu, J. Song, Z. Liu, Y. Huang, K. Huang, N. Tao, Z. Li, X. Bai, B. Li, M. Lei, Z. Yu and H. Wu, Direct spray-coating of highly robust and transparent Ag nanowires for energy saving windows, *Nano Energy*, 2019, **62**, 111–116.
34 B.-T. Liu and S.-X. Huang, Transparent conductive silver nanowire electrodes with high resistance to oxidation and thermal shock, *RSC Adv.*, 2014, **4**(103), 59226–59232.
35 A. R. Madaria, A. Kumar and C. Zhou, Large scale, highly conductive and patterned transparent films of silver nanowires on arbitrary substrates and their application in touch screens, *Nanotechnology*, 2011, **22**(24), 245201.
36 E. Marzbanrad, G. Rivers, P. Peng, B. Zhao and N. Y. Zhou, How morphology and surface crystal texture affect thermal stability of a metallic nanoparticle: the case of silver nanobelts and pentagonal silver nanowires, *Phys. Chem. Chem. Phys.*, 2015, **17**(1), 315–324.
37 M. T. Molares, V. Buschmann, D. Dobrev, R. Neumann, R. Scholz, I. U. Schuchert and J. Vetter, Single-crystalline copper nanowires produced by electrochemical deposition in polymeric ion track membranes, *Adv. Mater.*, 2001, **13**(1), 62–65.
38 V.-T. Nguyen and G. A. V. Phan, Atomistic insight into welding silver nanowires and interfacial characteristics of the welded zone, *Mater. Today Commun.*, 2023, **34**, 105051.
39 Q. Nian, M. Saei, Y. Xu, G. Sabyasachi, B. Deng, Y. P. Chen and G. J. Cheng, Crystalline nanojoining silver nanowire percolated networks on flexible substrate, *ACS Nano*, 2015, **9**(10), 10018–10031.
40 F. Niekiel, E. Spiecker and E. Bitzek, Influence of anisotropic elasticity on the mechanical properties of fivefold twinned nanowires, *J. Mech. Phys. Solids*, 2015, **84**, 358–379.
41 S. Nosé, A molecular dynamics method for simulations in the canonical ensemble, *Mol. Phys.*, 1984, **52**(2), 255–268.
42 M. Oh, W.-Y. Jin, H. J. Jeong, M. S. Jeong, J.-W. Kang and H. Kim, Silver nanowire transparent conductive electrodes for high-efficiency III-nitride light-emitting diodes, *Sci. Rep.*, 2015, **5**(1), 13483.
43 H.-K. Park, K. Y. Lee, J.-S. Seo, J.-A. Jeong, H.-K. Kim, D. Choi and S.-W. Kim, Charge-generating mode control in high-performance transparent flexible piezoelectric nanogenerators, *Adv. Funct. Mater.*, 2011, **21**(6), 1187–1193.
44 J. H. Park, G.-T. Hwang, S. Kim, J. Seo, H.-J. Park, K. Yu, T.-S. Kim and K. J. Lee, Flash-induced self-limited plasmonic welding of silver nanowire network for transparent flexible energy harvester, *Adv. Mater.*, 2017, **29**(5), 1603473.
45 J. J. Patil, W. H. Chae, A. Trebach, K.-J. Carter, E. Lee, T. Sannicolo and J. C. Grossman, Failing forward: Stability of transparent electrodes based on metal nanowire networks, *Adv. Mater.*, 2021, **33**(5), 2004356.
46 P. Peng, A. Hu and Y. Zhou, Laser sintering of silver nanoparticle thin films: microstructure and optical properties, *Appl. Phys. A*, 2012, **108**(3), 685–691.
47 S. Plimpton, Fast parallel algorithms for short-range molecular dynamics, *J. Comput. Phys.*, 1995, **117**(1), 1–19.
48 Q. Qin, S. Yin, G. Cheng, X. Li, T.-H. Chang, G. Richter, Y. Zhu and H. Gao, Recoverable plasticity in penta-twinned metallic nanowires governed by dislocation nucleation and retraction, *Nat. Commun.*, 2015, **6**(1), 5983.
49 V. V. Radmilović, M. Göbelt, C. Ophus, S. Christiansen, E. Spiecker and V. R. Radmilović, Low temperature solid-state wetting and formation of nanowelds in silver nanowires, *Nanotechnology*, 2017, **28**(38), 385701.
50 A. R. Rathmell, S. M. Bergin, Y.-L. Hua, Z.-Y. Li and B. J. Wiley, The growth mechanism of copper nanowires and their properties in flexible, transparent conducting films, *Adv. Mater.*, 2010, **22**(32), 3558–3563.
51 T. Sannicolo, N. Charvin, L. Flandin, S. Kraus, D. T. Papanastasiou, C. Celle, J.-P. Simonato, D. Munoz-Rojas, C. Jiménez and D. Bellet, Electrical mapping of silver nanowire networks: a versatile tool for imaging network homogeneity and degradation dynamics during failure, *ACS Nano*, 2018, **12**(5), 4648–4659.
52 T. Schneider and E. Stoll, Molecular-dynamics study of a three-dimensional one-component model for distortive phase transitions, *Phys. Rev. B*, 1978, **17**(3), 1302.
53 D. Sheppard, R. Terrell and G. Henkelman, Optimization methods for finding minimum energy paths, *J. Chem. Phys.*, 2008, **128**(13), 134106.
54 T.-B. Song, Y. Chen, C.-H. Chung, Y. Yang, B. Bob, H.-S. Duan, G. Li, K.-N. Tu, Y. Huang and Y. Yang, Nanoscale Joule heating and electromigration enhanced ripening of silver nanowire contacts, *ACS Nano*, 2014, **8**(3), 2804–2811.
55 J. A. Spechler and C. B. Arnold, Direct-write pulsed laser processed silver nanowire networks for transparent conducting electrodes, *Appl. Phys. A*, 2012, **108**, 25–28.
56 A. Stukowski, Visualization and analysis of atomistic simulation data with OVITO–the Open Visualization Tool, *Modell. Simul. Mater. Sci. Eng.*, 2009, **18**(1), 015012.
57 A. Teymouri, E. Adabifiroozjaei, R. F. Webster, S. M. Hagh, X. Hao, M. A. Green and S. Pillai, Evidence of low-temperature joints in silver nanowire based transparent conducting layers for solar cells, *ACS Appl. Nano Mater.*, 2020, **3**(4), 3205–3213.
58 S. Vigonski, V. Jansson, S. Vlassov, B. Polyakov, E. Baibuz, S. Oras, A. Aabloo, F. Djurabekova and V. Zadin, Au nanowire junction breakup through surface atom diffusion, *Nanotechnology*, 2017, **29**(1), 015704.
59 H. Wang, Y. Wang and X. Chen, Synthesis of uniform silver nanowires from AgCl seeds for transparent conductive films via spin-coating at variable spin-speed, *Colloids Surf., A*, 2019, **565**, 154–161.

 

60 P. Williams, Y. Mishin and J. Hamilton, An embedded-atom potential for the Cu–Ag system, *Modell. Simul. Mater. Sci. Eng.*, 2006, **14**(5), 817.
61 X. Wu, S. Wang, Z. Luo, J. Lu, K. Lin, H. Xie, Y. Wang and J.-Z. Li, Inkjet printing of flexible transparent conductive films with silver nanowires ink, *Nanomaterials*, 2021, **11**(6), 1571.
62 Z. Wu, Z. Chen, X. Du, J. M. Logan, J. Sippel, M. Nikolou, K. Kamaras, J. R. Reynolds, D. B. Tanner, A. F. Hebard and A. G. Rinzler, Transparent, conductive carbon nanotube films, *Science*, 2004, **305**(5688), 1273–1276.
63 S. Yin, G. Cheng, G. Richter, H. Gao and Y. Zhu, Transition of deformation mechanisms in single-crystalline metallic nanowires, *ACS Nano*, 2019, **13**(8), 9082–9090.